



Al-modified Pd@mSiO₂ core-shell catalysts for the selective hydrodeoxygenation of fatty acid esters: Influence of catalyst structure and Al atoms incorporation

Xincheng Cao^{a,b,c,d}, Jiaping Zhao^{a,b,c,d}, Feng Long^{a,b,c,d}, Xiaolei Zhang^f, Junming Xu^{a,b,c,d,e,*}, Jianchun Jiang^{a,b,c,d,e,*}

^a Institute of Chemical Industry of Forest Products, Chinese Academy of Forestry, Nanjing 210042, China

^b Key and Open Lab. on Forest Chemical Engineering, Nanjing 210042, Jiangsu Province, China

^c National Engineering Lab. for Biomass Chemical Utilization, Nanjing 210042, China

^d Key and Open Lab. on Forest Chemical Engineering, SFA, Nanjing 210042, China

^e Co-Innovation Center of Efficient Processing and Utilization of Forest Resources, Nanjing Forestry University, China

^f Department of Chemical and Process Engineering, University of Strathclyde, UK

ARTICLE INFO

Keywords:

Core-shell structure
Aluminum atoms incorporation
Selective hydrodeoxygenation
Diesel-range alkanes
Sintering resistant

ABSTRACT

The development of robust catalysts for selective hydrodeoxygenation (HDO) of fatty acid esters is key for production of the diesel-range alkanes under mild conditions. Here, we report a stable and efficient HDO catalyst (Pd@Al_x-mSiO₂) that composed of inner uniformly dispersed metallic palladium core and the outer mesoporous silica shell doped with aluminum atoms. Using methyl palmitate as a model compound, Al-modified Pd@mSiO₂ catalyst (Pd@Al₃-mSiO₂) exhibited higher catalytic performance (98% conversion rate and 99% selectivity towards diesel-range alkanes) as compared with the Pd@mSiO₂ and conventional Pd/γ-Al₂O₃ catalysts (35% and 70% conversion rates, respectively) at 260 °C and 3.0 MPa H₂. Further, when using vegetable oils such as soybean and palm oils as raw materials, high yields of diesel-range alkanes (> 80 wt%) can be obtained under the mild conditions. The HDO reaction pathway was more dominant than the decarbonylation pathway when the reaction was catalyzed by Pd@Al₃-mSiO₂ catalyst, thereby reducing the loss of carbon atoms. Detailed characterization (²⁷Al NMR, NH₃-TPD, and in situ Py-FTIR) suggests that the incorporation of aluminum atoms brings not only Lewis acid sites, but also Brønsted acid sites via the formation of Si—OH—Al bonds. The synergy between the metallic Pd, Lewis- and Brønsted-acid sites is responsible for its high HDO activity under the mild conditions. Additionally, the core-shell structure enables fatty aldehyde intermediate preferentially adsorbed on the aluminum atoms in the outer silica shell and avoids direct contacting with metallic Pd, which inhibits the cleavage of C—C bonds to some extent. On the other hand, due to the protective effect of outer silica shell that inhibits the leaching and agglomeration of metallic Pd, the synthesized Pd@Al₃-mSiO₂ catalyst showed good stability with a slight loss (conversion decreased from 98% to 90%) over five cycles.

1. Introduction

With the continuous depletion and consumption of fossil fuels, the development of renewable and clean energy production has become increasingly important. Biodiesel derived from biomass conversion has attracted great attention due to its reusability and low emission of pollutants [1,2]. Currently, fatty acid methyl ester (FAME), as the first generation of biodiesel, has been produced with a large scale by transesterification and annual output exceeds 20 million tons [3]. However,

high oxygen content and cold filter plugging point issues make it difficult to application as a high-grade transportation fuel [4]. The second-generation biodiesel derived from the direct conversion of fatty acid esters can solve the issues of the FAME because the as-prepared biodiesel is long-chain alkanes (C₁₂-C₂₂) and does not contain any oxygen element [5].

To date, two catalytic hydrodeoxygenation (HDO) catalysts have been extensively reported for production of diesel-range alkanes from fatty acid esters. The first employs sulfide transition metal catalysts,

* Corresponding authors at: Institute of Chemical Industry of Forest Products, Chinese Academy of Forestry, Nanjing 210042, China.

E-mail addresses: xujunming@icifp.cn (J. Xu), jiangjc@icifp.cn (J. Jiang).

<https://doi.org/10.1016/j.apcatb.2022.121068>

Received 20 October 2021; Received in revised form 14 December 2021; Accepted 3 January 2022

Available online 5 January 2022

0926-3373/© 2022 Elsevier B.V. All rights reserved.

such as NiMoS₄ and CoMoS₄, but strict environmental regulations on the sulfur content of biofuels hinder its application [6–8]. The second relies on supported metal catalysts in a reduced state, such as supported Ni [9–11], Co [12,13], Cu [14], Pd [15,16], Pt [17] and Ir [18] catalysts. Compared with the non-precious catalysts with high metal loadings and harsh reaction conditions, noble catalysts seem to be attractive due to its high catalytic activity and mild reaction conditions. However, the problems of instability and deactivation due to the leaching and agglomeration of metal nanoparticles during the reactions greatly limit its development. Besides, these catalysts often favor the decarbonylation and/or decarboxylation, which leads to some carbon atoms loss [16]. Therefore, in the process of fatty acid esters conversion, developing a noble metal catalyst with good reusability and high HDO selectivity towards target products has turned into a great challenge.

To inhibit the leaching and agglomeration of noble metal catalysts, great efforts have been devoted to improve the catalyst stability and reusability, which includes developing catalysts with stronger electron interaction between nanoparticles and support [19,20], embedding active sites into controlled cavities or pore channel of pre-synthesized molecular sieves [21,22], and constructing core/yolk shell nanostructures by coating a layer of shell on the pre-synthesized nanoparticles [23–29]. Among these methods, designing a nanocatalyst into core/yolk shell structure is a promising method to improve catalyst stability, since it can prevent the migration and sintering of nanoparticles. On the other hand, it is known that catalyst acidity plays an important role in promoting the conversion of esters and improving the HDO selectivity of products [11,30]. For example, the synergy between the hydrogenation metal and Lewis acid sites has been demonstrated for promoting the conversion of fatty acids/esters [18,31], while Brønsted acid sites are beneficial to enhance the HDO selectivity of products [32]. However, traditional core-shell structured catalysts have weak acidity due to its neutral silicon framework, which greatly limits their application in the conversion of fatty esters.

Based on the above analysis and an inspiration of inserting aluminum atoms into the silica framework to increase catalyst acidity in the molecular sieve catalysts via formation of the Si—OH—Al bonds [33–35], a series of Pd@Al_x-mSiO₂ core-shell catalysts with different framework aluminum content were synthesized and applied to convert fatty acid esters into diesel-range alkanes. To shed light on the structure-activity relationship, the catalyst structure was characterized by detailed characterization (XRD, BET, TEM, HRTEM and ²⁷AlNMR), and associated with their intrinsic catalytic activity. Additionally, several crucial parameters such as aluminum content, catalyst stability, reaction temperature and H₂ pressure were also investigated. To the best of our knowledge, only few literatures were reported using core-shell-type catalysts for the conversion of fatty acid esters. This research provides a paradigm for the application of core-shell-type catalysts in the HDO of fatty acid esters.

2. Experimental section

2.1. Material

Cetyltrimethylammonium bromide (CTAB, 99%), tetraethyl orthosilicate (TEOS, 98%), ascorbic acid (> 99%), sodium aluminate (NaAlO₂, 98%), potassium tetrachloropalladate (K₂PdCl₄, 98%), methyl palmitate (95%), γ-Al₂O₃ were all purchased from Shanghai Macklin Company. Soybean and palm oils were purchased from commercial sources. All chemicals were used without any further treatment.

2.2. Catalyst preparation

The Pd@Al_x-mSiO₂ core-shell catalysts were synthesized through a facile one-pot method. Typically, CTAB (0.1 g), as a template agent due to its appropriate carbon chain length, was added into 45 mL deionized water and stirred at 95 °C for 0.5 h. Then, an aqueous solution of

K₂PdCl₄ (0.02 M, 5 mL) was slowly added to the mixture, and stirred at 95 °C for 1.0 h. Afterwards, ascorbic acid (0.1 M, 1.7 mL) was added, and the mixture gradually changed into black. After stirring at 95 °C for 1.0 h, a NaOH solution was introduced into the above mixture to adjust the pH to around 10–11, and then 0.4 mL of TEOS was added as silica precursor. The mixture was stirred at 95 °C for 3.0 h, at which Pd core coated with silica shells was formed. Subsequently, a certain amount of NaAlO₂ solution (0.05 M) was introduced into the above mixture and was stirred for 1.0 h. The gray product was collected by centrifugation, repeatedly washed by using the distilled water and absolute ethanol until no chloride and bromine ions were detected by AgNO₃ aqueous solution (1.0 M), and then dried at 80 °C for 12.0 h. The mesoporous silica shell was achieved by removing the template agent of CTAB at 500 °C calcination for 4.0 h in air. In order to obtain Pd@Al_x-mSiO₂ core-shell catalysts with hydrogenation activity, the calcined catalyst was reduced at 200 °C for 2.0 h in a H₂ atmosphere. The synthesized catalysts were denoted as the Pd@Al_x-mSiO₂, where x refers to the volume of NaAlO₂ solution. For comparison, the conventional Pd/γ-Al₂O₃ catalyst was prepared by impregnation method at the same Pd content as the Pd@Al₃-mSiO₂ catalyst, as described previously [32].

2.3. Catalyst characterization

In situ X-ray diffraction (XRD) patterns of catalysts were performed on a Panalytical Empyrean X-ray diffractometer using Cu Kα (λ = 0.15418 nm) radiation under N₂ flow to investigate the changes of metal nanoparticles and the thermal stability of the catalyst with increasing temperature. The XRD patterns were recorded in a 2θ angle ranging from 10° to 80° and the step size of 0.02°. The unknown diffraction peaks were identified by using the PDF-2 2018 database. Prior to test, the sample (50 mg) was pretreated at 100 °C for 30 min under N₂ flow. During in situ XRD experiment, the tested sample was heated stepwise (using a 5 °C/min heating rate) from room temperature to 600 °C. The XRD patterns were recorded at 25, 50, 100, 200, 300, 400, 500 and 600 °C. Specific surface areas were measured on a Micromeritics ASAP 2460 instrument. The transmission electron microscopy (TEM) images were obtained on JEOL JEM-2010 high-resolution electron microscope, and the accelerating voltage was at 200 kV. ²⁷Al and ²⁹Si MAS NMR were carried out on a Bruker AVANCE III 600M.

NH₃ temperature-programmed desorption (NH₃-TPD) was performed in Auto Chem II 2920 equipment (Micromeritics). Typically, approximately 100 mg of catalyst was pre-reduced at 200 °C for 1.0 h under flowing H₂, and then the catalyst was cooled to room temperature in a He flow. NH₃-TPD was performed under 10% NH₃/He flow for 0.5 h, and then the temperature was increased from 50 °C to 800 °C in a heating rate of 10 °C min^{−1}. In situ FTIR spectra of pyridine, methyl octanoate and octanal were performed on a Tensor 27 instrument with modified transmission FTIR cell. Detailed procedures of the in situ FTIR were described in [Supporting information](#).

2.4. Reactivity measurements and product analysis

The hydrodeoxygenation experiments of reactants were performed in a 50 mL stainless steel autoclave. Typically, 0.1 g of reactant, 0.03 g of the activated catalyst, and 10 mL of cyclohexane solvent were added into the reactor. Prior to reaction, the reactor was purged with H₂ (2.0 MPa) for three times to remove the inside air, and then was pressurized into 3.0 MPa H₂ at room temperature. Subsequently, the mixture was heated to 260 °C with stirring speed of 1000 rpm. After reaction, the liquid products were collected and analyzed by gas chromatography (GC, Agilent 7890A/5975C). Quantitative analysis of liquid product was performed by using Eicosane as internal standard. The detailed analysis and measured procedures were described in our prior work [32].

To ensure reproducibility of experimental data, every experiment was performed at least two times. The conversion and product selectivity are calculated as follows (1)–(2):

$$\text{Conversion} = \frac{\text{mol}_{\text{initial reactant}} - \text{mol}_{\text{unreacted reactant}}}{\text{mol}_{\text{initial reactant}}} \times 100\% \quad (1)$$

$$\text{Selec. (detec. products)} = \frac{\text{mol}_{\text{product}} \times n_{\text{C atoms in product}}}{\text{mol}_{\text{total C atoms of in detected liquid products}}} \times 100\% \quad (2)$$

where n is the number of C atoms. Taking methyl palmitate model compound as an example, the ratio of HDO/DCO (hydrodeoxygenation/ (decarboxylation + decarbonylation)) is calculated as follows (3) [36]:

$$\text{HDO/DCO} = \text{C}_{16}/\text{C}_{15} \times 100\% \quad (3)$$

where C_{15} and C_{16} are relative carbon moles of pentadecane and hexadecane, respectively.

3. Results and discussion

3.1. Investigations of catalyst structure and physicochemical properties

In this work, the core-shell structured $\text{Pd@Al}_x\text{-mSiO}_2$ catalysts were prepared via four steps (Scheme 1): (1) the synthesis of colloidal Pd nanoparticles using CTAB as the capping agent, (2) silica polymerization around the colloidal Pd cores under the suitable pH value, and the generation of as-synthesized Pd@SiO_2 catalyst, (3) incorporating Al atoms into the silica framework to produce $\text{Pd@Al}_x\text{-SiO}_2$ catalysts, (4) the removal of CTAB template agent and the reduction of the as-synthesized catalyst to obtain $\text{Pd@Al}_x\text{-mSiO}_2$ core-shell catalyst with mesopores and hydrogenation activity.

The core-shell structure and elemental composition of the $\text{Pd@Al}_x\text{-mSiO}_2$ catalysts were characterized by using TEM and HAADF-STEM. The $\text{Pd@Al}_3\text{-mSiO}_2$ was selected as the studied catalyst because it showed the best catalytic performance among the $\text{Pd@Al}_x\text{-mSiO}_2$ catalysts (See later). As shown in Fig. 1(e), the monodisperse spherical morphology and core-shell structure of the $\text{Pd@Al}_3\text{-mSiO}_2$ catalyst were confirmed. Compared with the $\text{Pd@Al}_3\text{-SiO}_2$ without removing CTAB templates (Fig. 1(a)), after calcination at 500 °C for 4.0 h in air, we clearly see the pore structure of the $\text{Pd@Al}_3\text{-mSiO}_2$ catalyst (Fig. 1(b)). This good connectivity between the inside Pd metal core and outside mesoporous silica shell would greatly promote the transfer of reactant in the $\text{Pd@Al}_3\text{-mSiO}_2$ catalyst during reactions. High-magnification image (HRTEM) (Fig. 1(c)) showed that the average diameter of the $\text{Pd@Al}_3\text{-mSiO}_2$ catalyst was about ~ 85 nm while the Pd core size was ~ 10 nm. Moreover, the opened mesoporous nanochannels with ~ 4.8 nm and a series of lattice fringes with a d-spacing of 0.226 nm were also observed by HRTEM image (Fig. 1(d)). The measured lattice fringes in the metal core were attributed to the (111) plane of the metallic Pd [37]. These confirmed that the $\text{Pd@Al}_x\text{-mSiO}_2$ core-shell catalysts that composed of an inner metallic Pd core and an outer mesoporous silica shell were successfully synthesized by the facile one-pot method.

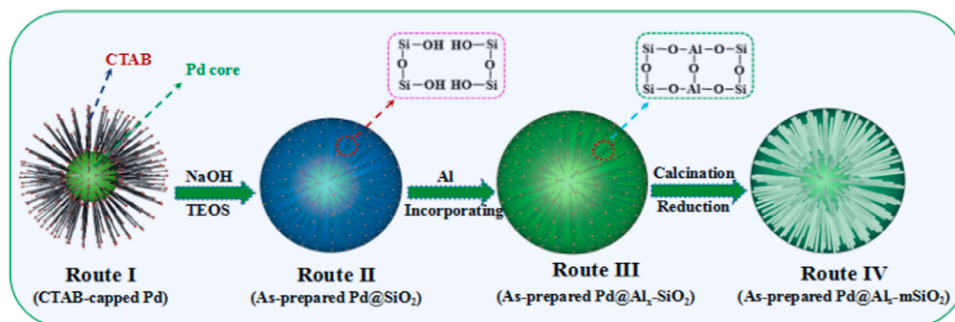
The different elemental distribution of the $\text{Pd@Al}_3\text{-mSiO}_2$ catalyst was investigated by HAADF-STEM-EDS. STEM and corresponding elemental mapping (Fig. 1(f)) showed that the isolated Pd metal core

was closely surrounded by silica shell with aluminum doping. This phase-separated in the $\text{Pd@Al}_3\text{-mSiO}_2$ catalyst can also be indicated by EDS line scan (Fig. 1(g)). Additionally, by studying the effect of aluminum content on the core-shell structure of the catalysts, it was found that, with an increase of aluminum content, the core-shell structure did not occur obvious changes as compared to Pd@mSiO_2 catalyst (See Fig. S1).

Nitrogen adsorption/desorption was conducted to determine the surface areas and pore structures of the synthesized catalysts. As shown in Fig. 2(a), the Pd@mSiO_2 and $\text{Pd@Al}_x\text{-mSiO}_2$ catalysts all presented the typical type-IV isotherm with a characteristic type-H1 hysteresis loops at $P/\text{Po} = 0.6\text{--}0.1$ [38], suggesting that the outer silica shell was mesoporous structure, which is consistent with the observation in the HRTEM images. The pore sizes of all tested samples were mainly distributed in the range of 2–6 nm (Fig. 2(b)), which also confirms that the catalysts are mesoporous structure. The parameters of the surface area, pore volume and pore diameters are listed in Table S1. As the aluminum species addition increased from 1.0 mL to 3.0 mL, the surface areas and pores of the catalysts did not occur obviously changes in comparison with the Pd@mSiO_2 catalyst. However, as further increased from 3.0 mL to 5.0 mL, the surface area and average pore size of the $\text{Pd@Al}_x\text{-SiO}_2$ catalysts ($\text{Pd@Al}_4\text{-mSiO}_2$ and $\text{Pd@Al}_5\text{-mSiO}_2$) gradually decreased, indicating that the optimum addition amount of the aluminum species was 3.0 mL. Combined the ^{27}Al NMR spectroscopy results (Fig. 3(a)), the decreased surface areas and average pore sizes in the $\text{Pd@Al}_4\text{-mSiO}_2$ and $\text{Pd@Al}_5\text{-mSiO}_2$ may be explained by the fact that in addition to a part of aluminum species incorporated into the silica framework, another part may be deposited on the surface and pores of the silica shell, and thus results in the decrease of surface areas and average pore sizes.

EDS mapping images (Fig. 1(f)) only reflect the distribution of different elements on the $\text{Pd@Al}_x\text{-mSiO}_2$ catalysts. It can not illustrate the coordinated state of different species and whether the Al atoms were inserted into silica framework. In order to analyze the local environments of Al species, ^{27}Al NMR spectroscopy was performed and the results are shown in Fig. 3(a). In the ^{27}Al NMR spectroscopy, the signals centered at 0 and 53 ppm were ascribed to octahedrally coordinated (AlO_6 structure unit) and tetra-coordinated aluminum (AlO_4 structure unit), respectively [39]. The 6-coordinated Al unit represented the extra-framework Al species, whereas the 4-coordinated Al unit represented the framework Al species. As shown in Fig. 3(a), with aluminum species increased from 2.0 to 3.0 mL, the signal of AlO_4 structure unit gradually enhanced. As the aluminum content further increased from 3.0 to 5.0 mL, however, the signal of AlO_6 structure unit gradually enhanced, which indicates that a part of aluminum species was deposited on the extra surface of silica shell and formed AlO_6 structure unit, namely extra-framework aluminum.

To further confirm that aluminum atoms were inserted into the silica framework of the $\text{Pd@Al}_x\text{-mSiO}_2$ catalysts, ^{29}Si NMR characterization was performed (Fig. 3(b)). Compared with the Pd@mSiO_2 catalyst with only one peak appeared at – 110 ppm (corresponding to Si (4Si, 0Al)),



Scheme 1. Schematic diagram of the $\text{Pd@Al}_x\text{-mSiO}_2$ catalysts prepared by one-pot method.

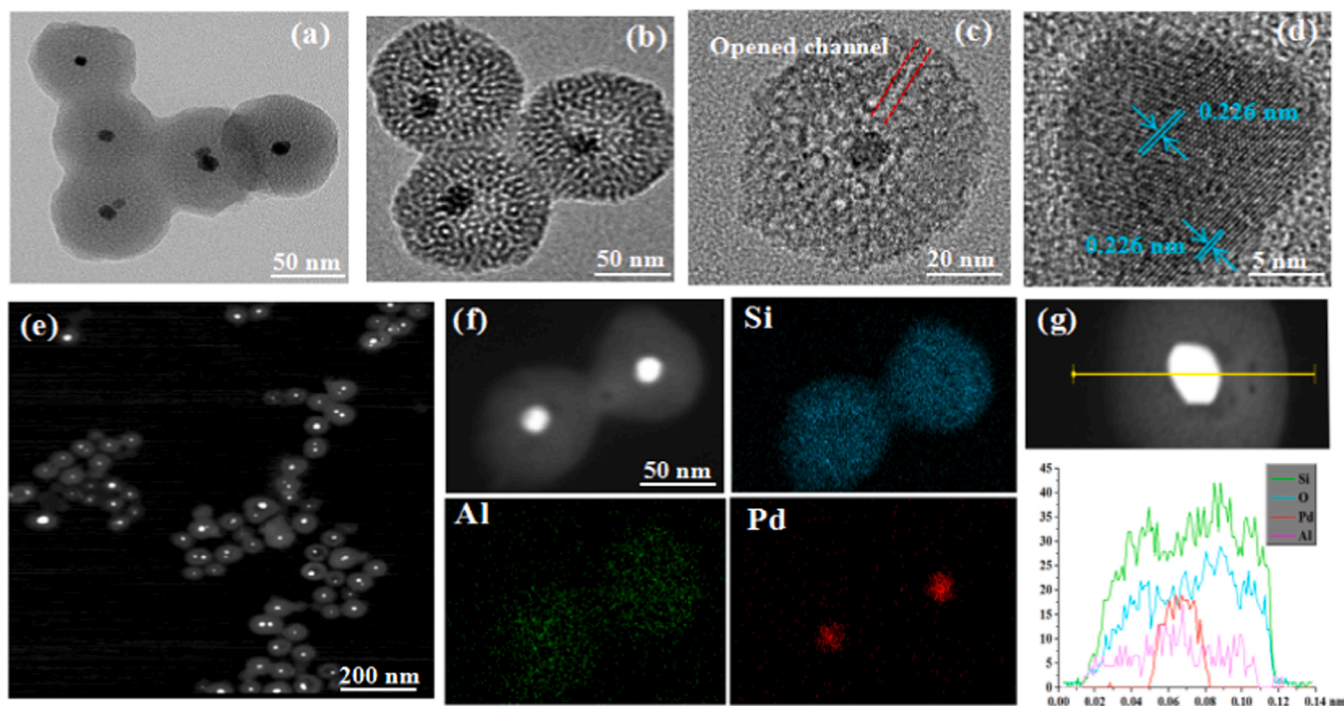


Fig. 1. (a) TEM image of Pd@Al₃-SiO₂ catalyst; (b) TEM image of Pd@Al₃-mSiO₂; (c) and (d) HRTEM images of Pd@Al₃-mSiO₂ catalyst; (e) and (f) STEM and corresponding STEM elemental mapping of Pd@Al₃-mSiO₂ catalyst, respectively; (g) HAADF-STEM line scanning of Pd@Al₃-mSiO₂ catalyst.

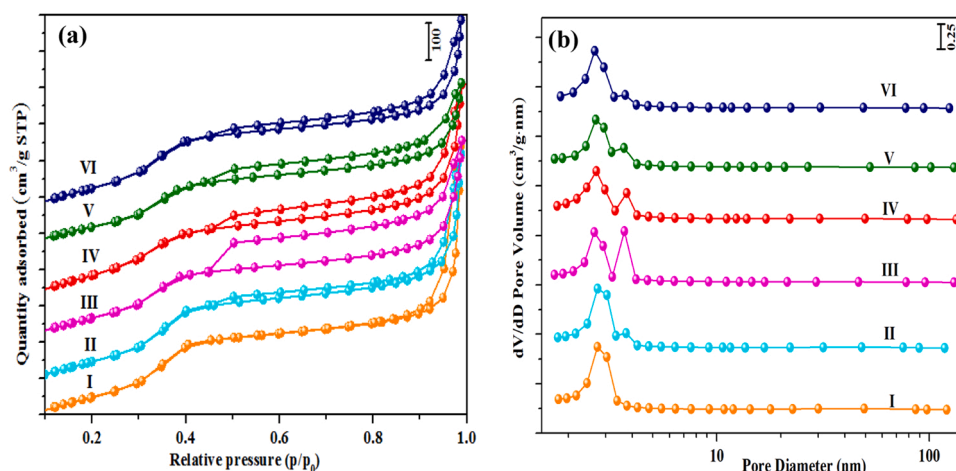


Fig. 2. (a) N₂ adsorption and desorption isotherm; (b) BJH pore size distribution curves: (I) Pd@mSiO₂; (II) Pd@Al₁-mSiO₂; (III) Pd@Al₂-mSiO₂; (IV) Pd@Al₃-mSiO₂; (V) Pd@Al₄-mSiO₂; (VI) Pd@Al₅-mSiO₂.

two new peaks located at -100 and -90 ppm were observed in the Pd@Al₃-mSiO₂ spectra, which corresponded to Si (3Si, 1Al) and Si (1Si, 3Al), respectively [40]. The above ²⁷Al and ²⁹Si NMR results suggest that the aluminum atoms are successfully incorporated into the silica framework of the Pd@Al_x-mSiO₂ catalysts and form the Si-OH-Al bonds.

According to prior literature [24,33], it is known that AlO₄ structure unit is helpful to increase the number of weak and medium acid sites, and thus influences the distribution of acid types because it forms Si-OH-Al bonds (See insert figure in Fig. 4(a)). In order to analyze the surface acidity of the Pd@mSiO₂ and Pd@Al_x-mSiO₂ catalysts, in-situ Py-FTIR and NH₃-TPD measures were performed. In the Py-FTIR spectra (Fig. 4(a)), the characteristic peaks appearing at approximately 1450 cm^{-1} and 1540 cm^{-1} were assigned to Lewis and Brønsted acid sites, respectively [41]. The adsorption peak appearing at approximately 1489 cm^{-1} was ascribed to both Lewis and Brønsted acid sites

[41]. As shown in Fig. 4(a), the Pd@mSiO₂ catalyst only showed Lewis acid sites, while the Pd@Al_x-mSiO₂ catalysts displayed both Lewis and Brønsted acid sites. With aluminum content increased from 1.0 to 5.0 mL, the amounts of the total acid sites gradually increased (Table 1). These results indicate that introducing aluminum species into the Pd@mSiO₂ catalyst enhanced the catalyst acidity, and generated Brønsted acid sites.

To investigate the acid strength, in-situ Py-FTIR of the Pd@Al₃-mSiO₂ catalyst was recorded. As shown in Fig. 4(b), after evacuation at $100\text{ }^{\circ}\text{C}$, the Pd@Al₃-mSiO₂ catalyst showed strong peak intensity at 1450 cm^{-1} (Lewis acid sites) and 1540 cm^{-1} (Brønsted acid sites). With the evacuation temperature increased, the intensity of these peaks gradually decreased. Notably, as the temperature increased to $300\text{ }^{\circ}\text{C}$, these peaks all disappeared, which indicates that the weak and medium acid sites were predominant in the Pd@Al₃-mSiO₂ catalyst.

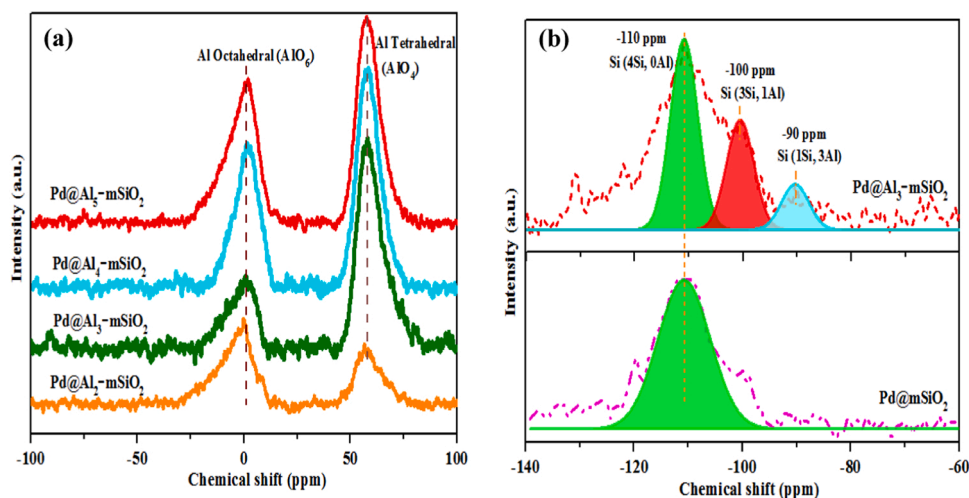


Fig. 3. (a) ^{27}Al NMR (b) ^{29}Si NMR spectroscopy of the $\text{Pd@Al}_x\text{-mSiO}_2$ catalysts.

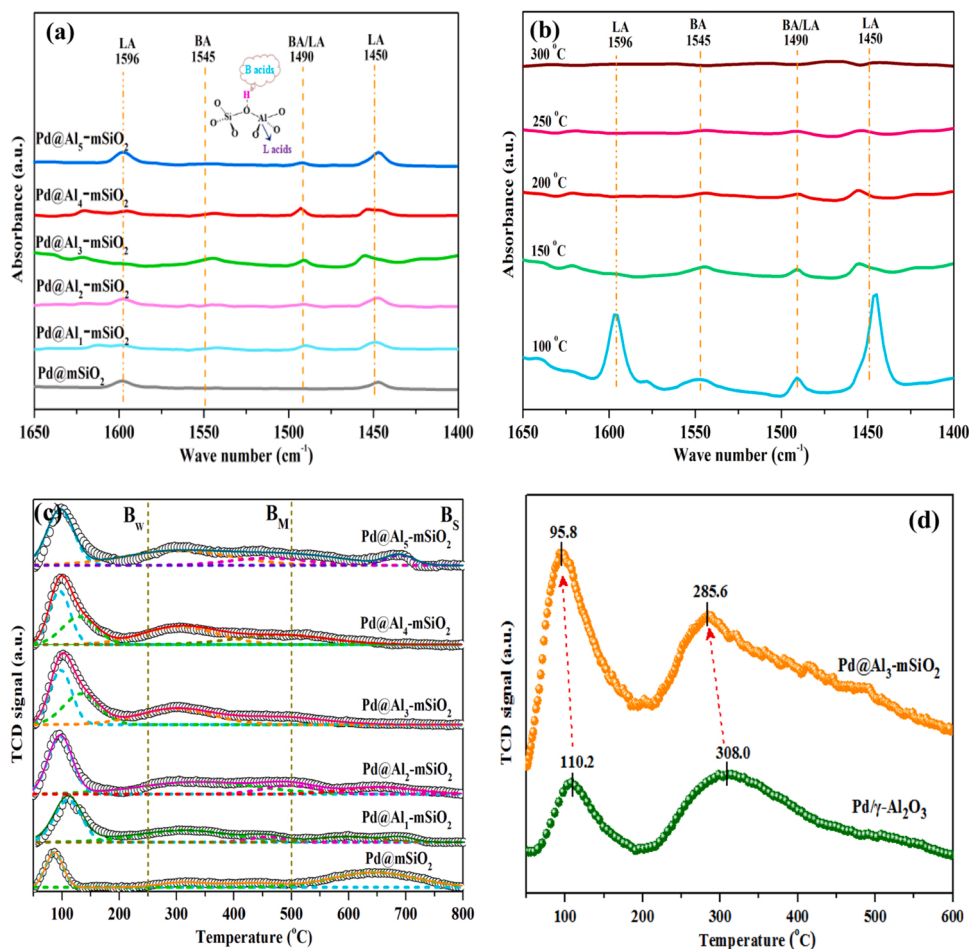


Fig. 4. (a) FTIR spectra of pyridine on various catalysts at 150 °C; (b) in situ FTIR spectra of pyridine on the $\text{Pd@Al}_3\text{-mSiO}_2$ catalyst at different temperatures; (c) NH_3 -TPD profiles of different catalysts; (d) H_2 -TPD profiles of $\text{Pd@Al}_3\text{-mSiO}_2$ and $\text{Pd}/\gamma\text{-Al}_2\text{O}_3$ catalysts.

Additionally, NH_3 -TPD was conducted to further determine the acid strength of the Pd@mSiO_2 and $\text{Pd@Al}_x\text{-mSiO}_2$ catalysts. According to the NH_3 desorption temperature, the acid sites were divided into weak (100–250 °C), medium (250–500 °C) and strong acid sites (> 500 °C) [42]. As shown in Fig. 4(c), the Pd@mSiO_2 catalyst only showed a weak peak centered at 100 °C, while the $\text{Pd@Al}_x\text{-mSiO}_2$ ($x = 1\text{--}4$) catalysts showed two NH_3 desorption temperature centered at 100 °C and 265 °C,

ascribing to the weak and medium acid sites, respectively. As for the $\text{Pd@Al}_5\text{-mSiO}_2$ catalyst, a novel NH_3 desorption peak was observed in the temperature range 600–700 °C, which was attributed to the strong acid sites. According to the results listed in Table 1, it is known that the $\text{Pd@Al}_3\text{-mSiO}_2$ catalyst had more weak and medium acid sites as compared with other $\text{Pd@Al}_x\text{-mSiO}_2$ catalysts.

For the hydrogenation reactions, the ability to activate and dissociate

Table 1
Acid distributions of different catalysts.

Entry	Catalyst	BA ^a (mmol g ⁻¹)	LA ^a (mmol g ⁻¹)	Acid Sites (mmol g ⁻¹)		
				B _W ^b	B _M ^b	B _T ^b
1	Pd@mSiO ₂	0.001	0.032	0.211	0.091	0.308
2	Pd@Al ₁ -mSiO ₂	0.012	0.053	0.654	0.307	0.965
3	Pd@Al ₂ -mSiO ₂	0.020	0.067	0.632	0.574	1.206
4	Pd@Al ₃ -mSiO ₂	0.053	0.085	0.850	0.623	1.473
5	Pd@Al ₄ -mSiO ₂	0.032	0.102	0.769	0.678	1.450
6	Pd@Al ₅ -mSiO ₂	0.025	0.128	0.589	0.827	1.456

^a BA and LA are the concentration of Brønsted and Lewis acid sites determined by Py-FTIR at 150 °C, respectively.

^b B_W, B_M, and B_T are the concentration of weak, medium, and total acid sites determined by NH₃-TPD, respectively.

hydrogen is important for the hydrogenation catalysts. To study the ability of the Pd@Al₃-mSiO₂ catalyst, H₂-TPD experiment was carried out. For comparison, the conventional Pd/γ-Al₂O₃ catalyst was also tested. As shown in Fig. 4(d), compared with the Pd/γ-Al₂O₃ catalyst, the H₂ desorption peaks of Pd@Al₃-mSiO₂ catalyst all shifted to lower temperatures and both peak area and peak intensity increased. This result indicates that Pd@Al₃-mSiO₂ catalyst is easier to activate and dissociate H₂ than the Pd/γ-Al₂O₃ catalyst, and therefore contribute to the improvement of catalytic activity.

The thermal stability of the Pd/γ-Al₂O₃ and Pd@Al₃-mSiO₂ was analysed by using in-situ XRD in the temperature range 25–600 °C under N₂ atmosphere. Although these catalysts were tested under N₂

atmosphere, it is inevitable that the metal nanoparticles are oxidized during the heating process, especially in the high temperature environment. As shown in Fig. 5(a), at room temperature (25 °C), the characteristic diffraction peaks of metallic Pd (JCPDS 46-1043) were observed in the XRD pattern of the Pd/γ-Al₂O₃ catalyst. As test temperature increased from 25 to 300 °C, the peak intensity corresponding to Pd metal at 2θ = 50.2° did not occur obviously changes. But, when the temperature increased from 300 to 400 °C, the diffraction peaks of the PdO (JCPDS 41-1107) were detected and the peak intensity gradually became strong as temperature increased. The Pd metal was completely oxidized into PdO at 600 °C. This result indicates that the dispersed Pd metal nanoparticles on the surface of Pd/γ-Al₂O₃ catalyst were easily oxidized and sintered at high temperatures, which affects catalytic activity. In contrast, the Pd@Al₃-mSiO₂ core-shell catalyst preserved its XRD peak intensity, and only minor Pd metal was oxidized into PdO nanoparticles even temperature up to 600 °C (Fig. 5(b)). This result indicates that the synthesized Pd@Al₃-mSiO₂ core-shell catalyst not only has high thermal stability, but also has good oxidation resistance at high temperatures. In order to observe the changes of Pd metal at different temperatures, TEM images were made (Fig. 5(c-f)). As the treated temperature increased from 25 to 600 °C, the Pd@Al₃-mSiO₂ catalyst maintained its core-shell structure and the metallic palladium particles were rarely aggregated (Fig. 5(c) and (d)), whereas the Pd/γ-Al₂O₃ catalyst appeared obviously agglomeration (Fig. 5(e) and (f)). This result demonstrates that the unique structure of the Pd@Al₃-mSiO₂ make it have good resistance to sintering and agglomeration at high operating temperatures.

3.2. Catalyst activity

In order to select the optimum HDO catalyst, catalytic performances

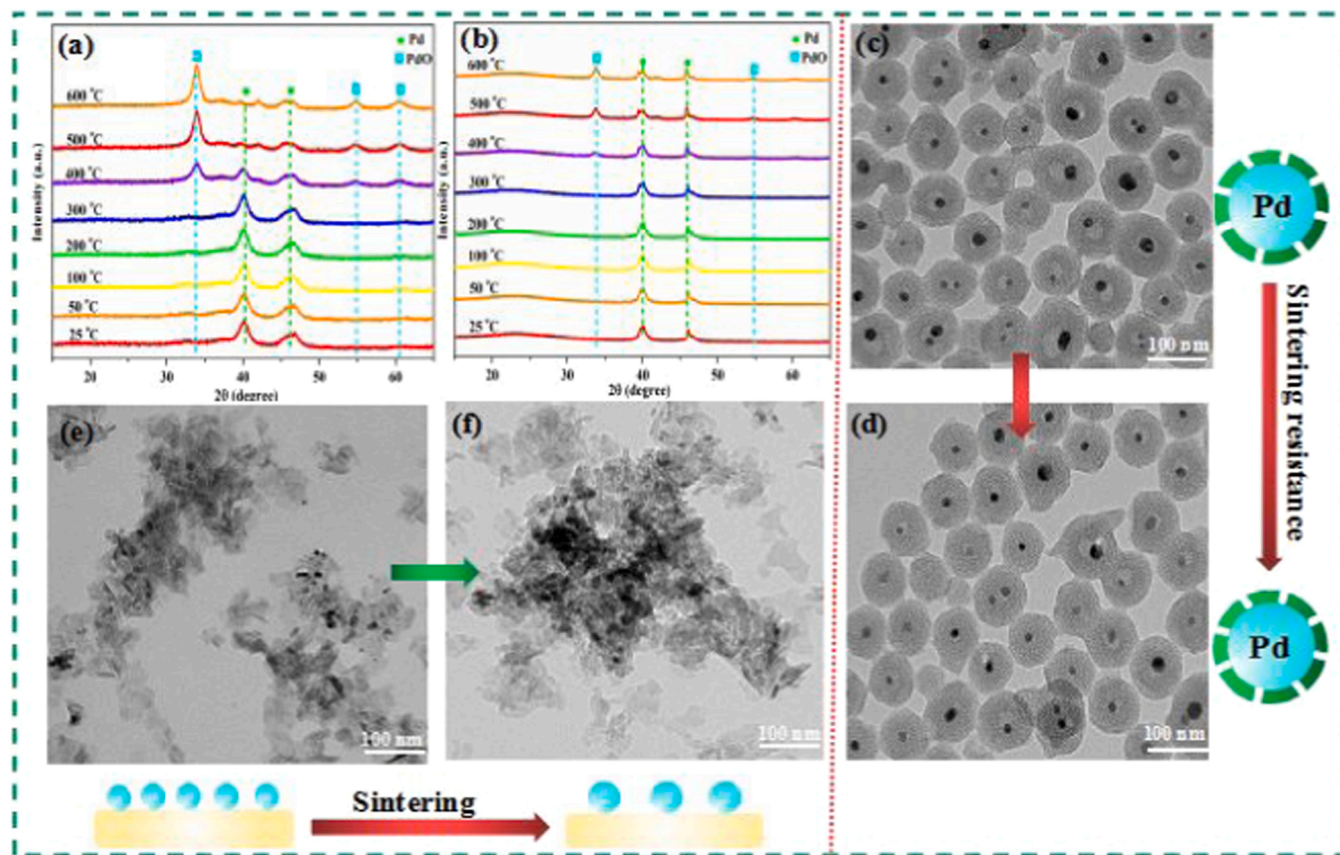


Fig. 5. In situ XRD patterns of Pd/γ-Al₂O₃ (a) and Pd@Al₃-mSiO₂ (b) catalysts; TEM images of (c) Pd@Al₃-mSiO₂ (25 °C); (d) Pd@Al₃-mSiO₂ (600 °C); (e) Pd/γ-Al₂O₃ (25 °C); (f) Pd/γ-Al₂O₃ (600 °C).

of the different catalysts were evaluated in the conversion of methyl palmitate. As shown in Fig. 6, under the identical reaction conditions (260 °C and 3.0 MPa H₂ pressure), Pd@mSiO₂ catalyst showed a low catalytic activity (35% conversion), while the Pd@Al_x-mSiO₂ catalysts with different aluminum contents showed excellent catalytic performance (> 80% conversion), where the main products were C₁₅, C₁₆ alkanes and minor amount of cetyl alcohol (C₁₆-OH). This indicates that the introduction of aluminum species greatly improved the catalytic activity. With aluminum content increased, the conversion of methyl palmitate first increased from 82% of Pd@Al₁-mSiO₂ to the maximum value of 98% for the best Pd@Al₃-mSiO₂ catalyst, and then gradually declined to 92% for the Pd@Al₅-mSiO₂. According to the characteristic results of BET (Table S1), the reason for the decreased catalytic performance of the Pd@Al₄-mSiO₂ and Pd@Al₅-mSiO₂ catalysts was mainly attributed to the reduction of surface areas and average pore sizes, which could decrease the mass transfer efficiency of the reactant. Table S2 shows the performance of Pd@Al₃-mSiO₂ catalyst and comparison with the previous published studies. The Pd@Al₃-mSiO₂ catalyst showed excellent catalytic performance for production of alkanes from the conversion of fatty acid esters under the mild reaction temperature of 260 °C. Moreover, compared with the conventional supported Pd metal catalysts (Pd/BaSO₄ and Pd/MWCNTs listed in Table S2) that exhibits a low HDO/DCO ratio (< 0.1), the Pd@Al₃-mSiO₂ catalyst showed a high HDO/DCO ratio (2.5). These results demonstrate that the Pd@Al₃-mSiO₂ catalyst has excellent catalytic performance and HDO selectivity in the conversion of fatty acid esters.

By calculating HDO/DCO ratio, it was found that the Pd@Al_x-mSiO₂ catalysts showed higher ratio value (HDO/DCO > 0.9) in comparison with the Pd@mSiO₂ catalyst (HDO/DCO = 0.2). With the aluminum content increased, the ratio value exhibited first increasing and then decreasing trend. The maximum value (HDO/DCO = 2.5) was obtained over the Pd@Al₃-mSiO₂ catalyst. For comparison, under the identical conditions, the catalytic performance of Pd/γ-Al₂O₃ catalyst prepared by impregnated method was also studied, and the results showed that it exhibited a medium catalytic performance with 70% conversion rate. Moreover, a low HDO/DCO ratio value (HDO/DCO < 0.1) suggested that the decarbonylation was dominant over the Pd/γ-Al₂O₃ catalyst.

Reaction temperature would have a great effect on the catalytic performance and HDO/DCO ratio value. Therefore, with the optimum

catalyst of Pd@Al₃-mSiO₂ catalyst, the catalytic activity and HDO/DCO ratio value were studied in the temperature range 220–280 °C (Fig. 7(a)). The conversion of methyl palmitate increased rapidly from 220 °C (33%) to 260 °C (98%), and remained unchanged in the range 260–280 °C (100%). In the selected temperature ranges (220–280 °C), the main products were alkane products (C₁₅ and C₁₆ alkanes). The HDO/DCO ratio value displayed a gradual decreasing trend as reaction temperature increased, revealing that high temperatures are unfavorable for the hydrodeoxygenation selectivity of products. The ratio value was always greater than one in the selected temperatures, suggesting that the hydrodeoxygenation reaction pathway always dominates over the Pd@Al₃-mSiO₂ catalyst. For comparison, the catalytic performance of Pd/γ-Al₂O₃ catalyst was also evaluated with respect to reaction temperature. As shown in Fig. 7(a), the Pd/γ-Al₂O₃ catalyst showed medium catalytic activity (70% conversion rate) at 260 °C, and the methyl palmitate was completely converted at ≥ 280 °C. Besides, in the selected temperatures, the low HDO/DCO values (< 0.5) indicate that the decarbonylation reaction was always dominant on the Pd/γ-Al₂O₃ catalyst. These results suggest that the Pd@Al₃-mSiO₂ catalyst has higher catalytic activity than the conventional Pd/γ-Al₂O₃ catalyst at a low temperature of 260 °C (98% VS 70% conversion), but also it mainly removes the oxygen atoms of fatty esters through HDO reaction pathway.

In order to obtain the optimized reaction parameters for oils conversion, other reaction conditions, such as H₂ pressure and reaction times, were also studied. As shown in Fig. 7(b), the effect of initial hydrogen pressure on the conversion of methyl palmitate and the alkanes selectivity was not significant as that of reaction temperature. But, initial H₂ pressure has a great influence on the HDO/DCO value. In contrast to the decrease of HDO/DCO value caused by high reaction temperatures, the HDO/DCO value exhibited increasing trend with initial hydrogen pressure increasing from 1.0 to 3.0 MPa. Further increasing H₂ pressure to 4.0 MPa did not result in obvious changes in product distribution, suggesting that the optimized H₂ pressure was 3.0 MPa. Fig. 7(c) showed that the optimal reaction time was 5.0 h, in which the reactant was basically converted and the alkanes selectivity was as high as 98%. Based on the above results and the principle of minimum energy consumption, the Pd@Al₃-mSiO₂ catalyst, 260 °C of reaction temperature, 3.0 MPa of H₂ pressure and 5.0 h of reaction time were chosen.

Under the optimum catalyst and reaction conditions, the vegetable oils such as soybean oil and palm oil were hydrotreated to produce diesel-range alkanes (Fig. 7(d)). The composition of these vegetable oils was listed in Table S3. Under the selected reaction conditions, a high yield of diesel-range alkanes (84.3 wt% and 82.5 wt%, respectively) from the conversion of the two oils were obtained over the Pd@Al₃-mSiO₂ catalyst, and these values are close to the theoretical values (soybean oil: 86.4 wt%; palm oil: 85.2 wt%) [15]. Moreover, it was found that the side reaction of the C—C bond cleavage was largely suppressed and only a small amount of cracking products were obtained (< 3 wt%) due to the low operating temperature of 260 °C. These results indicate that the Pd@Al₃-mSiO₂ catalyst is a promising catalyst which realizes the low-temperature deoxygenation of vegetable oils to produce the diesel-range alkanes.

Fig. 8(a) shows the reusability of the Pd@Al₃-mSiO₂ catalyst in the conversion of methyl palmitate. After the first run, the catalyst was obtained by centrifugation, dried at 80 °C, and then directly used the next run. As shown in Fig. 8(a), after recycling five runs, the catalytic activity of Pd@Al₃-mSiO₂ showed a slight loss (conversion decreased from 98% to 90%) while the selectivity of alkanes remained above 95%. These results suggest that the synthesized Pd@Al₃-mSiO₂ core-shell-type catalyst has good reusability. The XRD and TEM characteristic measures (Fig. 8(b) and (c)) were conducted to explore the structure of the spent catalyst. After the fifth recycling test, the XRD patterns of the spent Pd@Al₃-mSiO₂ catalyst revealed that the diffraction peaks assigning to Pd metal were almost no obvious changes in comparison with the fresh

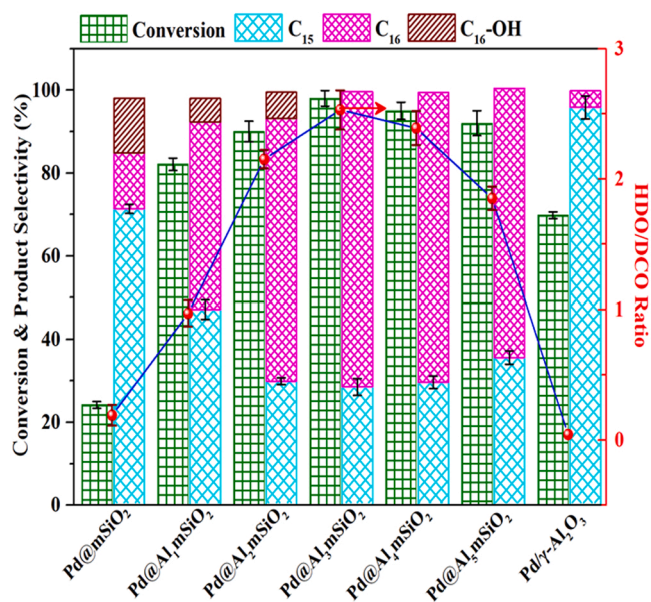


Fig. 6. Conversion of methyl palmitate and product distributions over various catalysts. Reaction conditions: 0.03 g of catalyst; 0.1 g of reactant in 10 mL solvent at 260 °C and 3.0 MPa H₂ for 5.0 h.

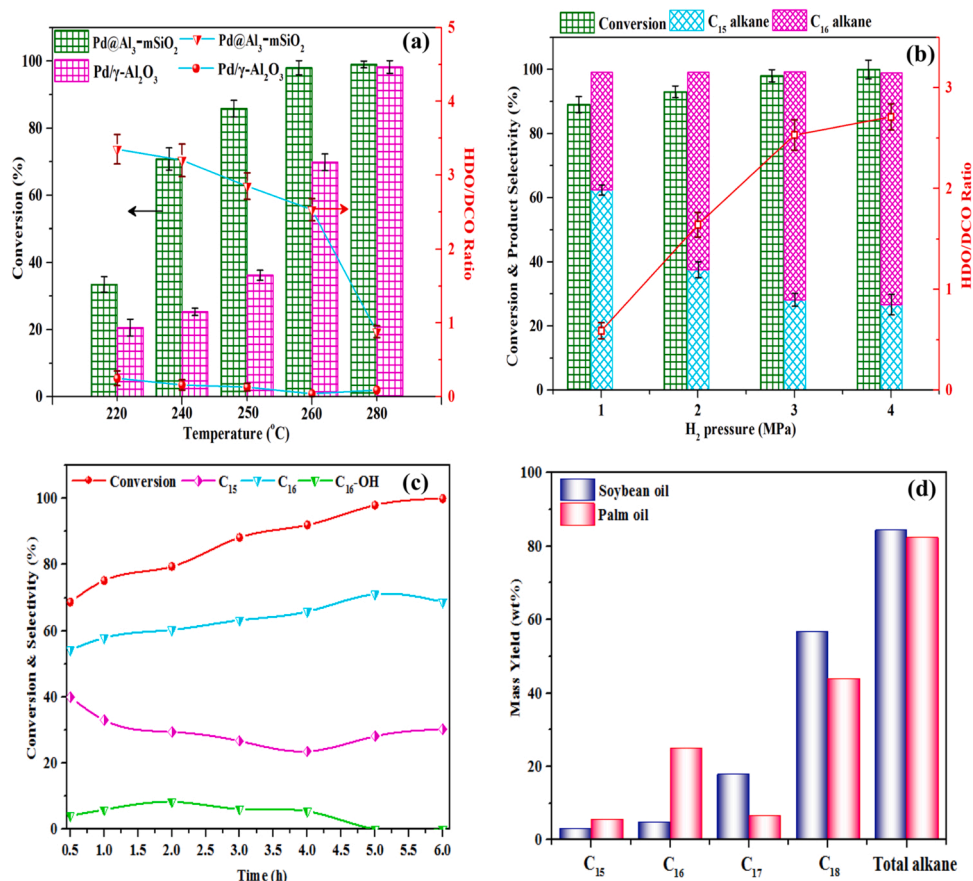


Fig. 7. (a) Comparison of catalytic performance between the Pd/γ-Al₂O₃ and Pd@Al₃-mSiO₂ catalysts as a function of reaction temperature; (b) effect of H₂ pressure on the conversion of methyl palmitate; (c) reaction composition-time profile for the conversion of methyl palmitate; (d) product distributions obtained from the conversion of soybean oil and palm oil. General conditions: 0.03 g of catalyst; 0.1 g of reactant in 10 mL solvent at 260 °C and 3.0 MPa H₂ for 5.0 h.

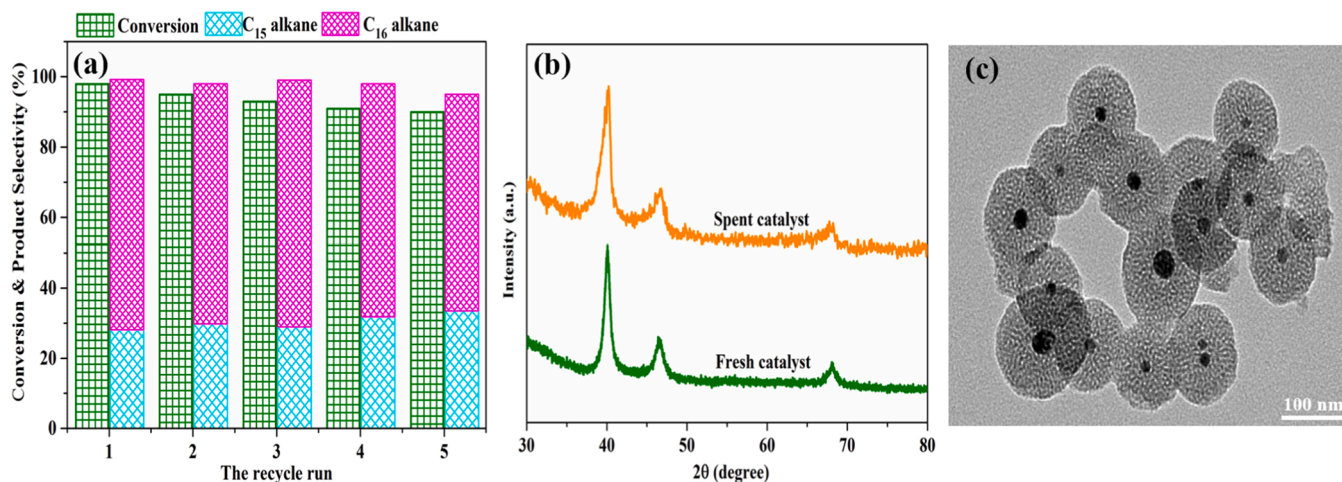


Fig. 8. (a) Recyclability of the Pd@Al₃-mSiO₂ catalyst; (b) XRD patterns of the spent and fresh catalysts; (c) TEM image of the spent catalyst. Reaction conditions: reactant (0.1 g), catalyst (0.03 g), cyclohexane (10 mL), 260 °C, initial H₂ pressure (3.0 MPa).

catalyst. TEM images showed that the spent Pd@Al₃-mSiO₂ catalyst preserved its core-shell structure and no obvious metal agglomeration was observed. Based on the in-situ XRD and TEM images, we concluded that the good stability of the Pd@Al₃-mSiO₂ catalyst could be attributed to its unique core-shell structure, where the silica shell prevents the leaching of Pd element and inhibits the agglomeration of metal nanoparticles at high temperatures.

3.3. Analysis of the structure-activity relationship

According to the above results, a question we can raise is why the synthesized Pd@Al₃-mSiO₂ catalyst has higher catalytic activity and HDO/DCO value than the Pd@mSiO₂ and Pd/γ-Al₂O₃ catalysts at a low temperature of 260 °C. Apparently, there are two main factors that affect these values, i.e., the strong synergistic effect of the metal-oxide and the type of acid sites. At the Pd-Al interface, H₂ was dissociated

into active hydrogen atoms over the metallic Pd sites, while the carbonyl group of fatty esters was adsorbed and activated over the Al^{3+} sites. The active hydrogen atoms transferred to Al sites via spillover effects and hydrogenated the adsorbed fatty esters to form fatty aldehyde intermediate. Subsequent, the resulting fatty aldehyde intermediate was converted into alkanes via two parallel reaction pathways: either via decarbonylation to produce RH alkanes, or via hydrogenation to produce fatty alcohols, and then produce RCH_3 alkanes through dehydrated-hydrogenation process under the action of Brønsted acids and Pd metal. In contrast to the conventional Pd/ $\gamma\text{-Al}_2\text{O}_3$ catalyst, uniformly dispersed metallic Pd nanoparticles (providing more active hydrogen atoms as proved in H_2 -TPD (Fig. 4(d))), strong interaction between the reactant and the interface of Pd-Al, and abundant the number of Brønsted acid sites of the Pd@ $\text{Al}_3\text{-mSiO}_2$ make it have higher catalytic activity and HDO/DCO value.

To confirm the speculation, in situ FTIR of the methyl octanoate was performed. Methyl octanoate was selected as the probe molecule because of its low boiling points and similar functional groups to long-chain fatty esters. As shown in Fig. 9(a), the band at 1750 cm^{-1} was attributed to the vibration modes of $\nu(\text{C}=\text{O})$ [43,44], while the bands at $2990\text{--}2885\text{ cm}^{-1}$ were ascribed to the stretching frequencies of the aliphatic C-H (CH_3 , CH_2 , and CH) [17,45]. Noted that the spectrum of methyl octanoate adsorbed on the Pd@mSiO₂ and Pd/ $\gamma\text{-Al}_2\text{O}_3$ catalysts displayed weak bands at 100°C , which cannot be detected when the temperature increased to 130°C (Fig. 9(a) and (b), respectively). In contrast, the characteristic band ($\text{C}=\text{O}$) of methyl octanoate was still observed on the Pd@ $\text{Al}_3\text{-mSiO}_2$ catalyst even at 130°C (Fig. 9(c)). These

suggest that methyl octanoate has a stronger interaction with the Pd@ $\text{Al}_3\text{-mSiO}_2$ catalyst than that of the Pd/ $\gamma\text{-Al}_2\text{O}_3$ and Pd@mSiO₂ catalysts. Additionally, chemical adsorption of methyl octanoate was observed on the Pd@ $\text{Al}_3\text{-mSiO}_2$ and Pd/ $\gamma\text{-Al}_2\text{O}_3$ catalysts, where the characteristic band shifted to higher wavenumbers. In contrast, this chemical shift was not observed on the Pd@mSiO₂ catalyst. These results revealed that the Al^{3+} active sites in the Pd@ $\text{Al}_3\text{-mSiO}_2$ and Pd/ $\gamma\text{-Al}_2\text{O}_3$ catalysts play an important role in adsorbing and activating carbonyl group of fatty esters, and the strongest interaction occurred on the surface of the Pd@ $\text{Al}_3\text{-mSiO}_2$ catalyst.

To investigate the adsorption mode of fatty aldehyde intermediate on the surface of Pd@ $\text{Al}_3\text{-mSiO}_2$, in situ FTIR of octanal was performed (Fig. 9(d)). The $\text{C}=\text{O}$ stretching band of the octanal was observed at 1720 cm^{-1} , and the characteristic band shifted to lower wavenumbers with temperature increased. Besides, the appearance of the band at 1405 cm^{-1} , an indicator of bicoordination adsorption of carbonyl carbon and oxygen atoms in fatty aldehyde (denoted as di- $\sigma_{\text{C,O}}$ configuration) [46], indicates that the octanal was chemically adsorbed on the surface of Pd@ $\text{Al}_3\text{-mSiO}_2$ catalyst in a mode of di- $\sigma_{\text{C,O}}$ configuration via $\text{C}=\text{O}$ bonds. These results suggest that there is an interaction between the fatty aldehyde intermediate and the Pd-Al interface, i.e., the carbonyl carbon and oxygen atoms in fatty aldehyde were bonded on the Pd and Al active sites, respectively.

To study why the Pd@ $\text{Al}_3\text{-mSiO}_2$ catalyst exhibited high HDO/DCO value, we normalized the HDO/DCO value as a function of B acid sites (Fig. S2). As the number of B acid sites increases, the HDO/DCO value exhibits an increasing trend. This indicates that B acid sites play an

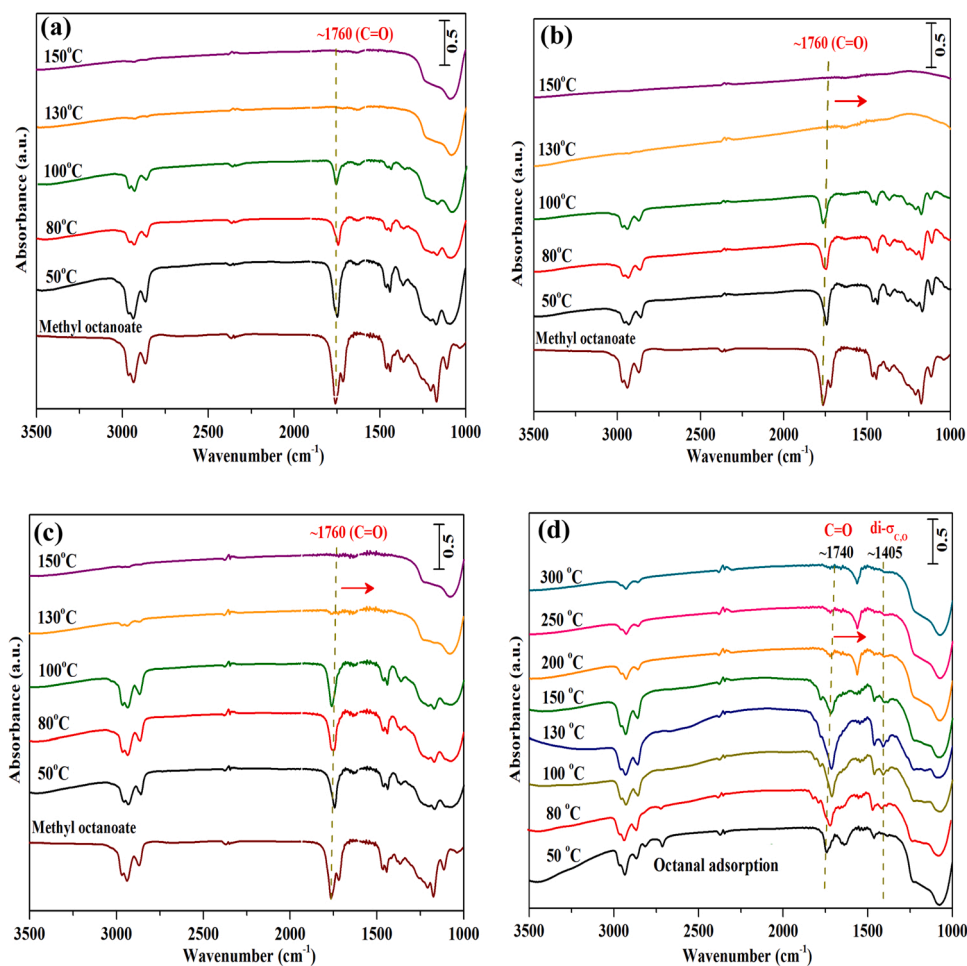


Fig. 9. In situ FTIR for the methyl octanoate adsorption over the Pd@mSiO₂ (a); Pd/ $\gamma\text{-Al}_2\text{O}_3$ (b); Pd@ $\text{Al}_3\text{-mSiO}_2$ (c); and for the octanal adsorption over the Pd@ $\text{Al}_3\text{-mSiO}_2$ (d).

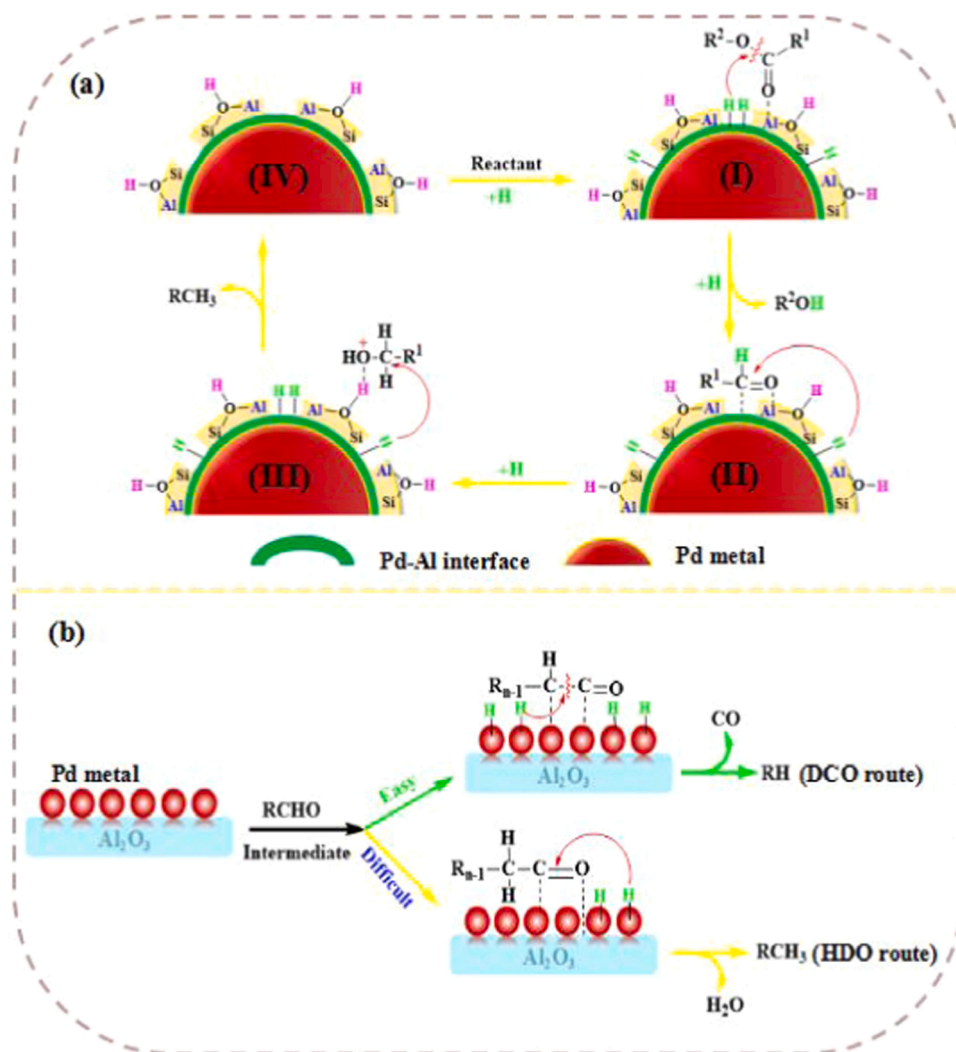
important role in improving the HDO/DCO value. From Fig. S2, it was found that the HDO/DCO value was not linear relationship with the increase of B acid sites, which reveals that B acid sites are not an exclusive factor for improving the HDO/DCO value. Considering the unique structure of the Pd@Al₃-mSiO₂ catalyst, we believe that the high HDO/DCO value may be associated with its unique core-shell structure.

The core-shell structure that composed of the inner Pd metal core and the outer silica shell containing Al active sites enables the fatty aldehyde intermediate first to be adsorbed on the Al sites, and then contacts with inner Pd metal core. This leads fatty aldehyde intermediate to adsorb on the Pd-Al interface in a mode of di- $\sigma_{C,O}$ configuration to produce fatty alcohols (Scheme 2(a) (II)) (as proved in Fig. 9(d)), followed by generating alkanes via the dehydrated-hydrogenation process under the action of Brønsted acid sites and Pd metal (Scheme 2(a) (III)). In contrast, on the surface of the Pd/ γ -Al₂O₃ catalyst (Scheme 2(b)), since the metallic Pd is exposed on the surface of the Al₂O₃ support, the fatty aldehyde is easily adsorbed on the Pd metal surface through C-C bonds, which results in the cleavage of C-CHO bonds to produce alkane with one carbon atom less (Scheme 2(b) (DCO route)). Additionally, since the Pd/ γ -Al₂O₃ catalyst contains minor B acid sites (0.001 mmol g⁻¹ determined by Py-FTIR at 150 °C), the generating fatty alcohol is more easier to occur dehydrogenation than the dehydration reaction on the exposed metallic Pd sites, which produced fatty aldehydes. Subsequently, the generated fatty aldehyde produced alkanes by

decarbonylation reaction, which results in a low HDO/DCO ratio value. Based on the above results and analysis, we concluded that under mild conditions (260 °C and 3.0 MPa H₂ pressure), the high catalytic activity of the Pd@Al₃-mSiO₂ catalyst was attributed to its excellent ability of H₂ dissociation/activation and strong interaction between the reactant and the Pd-Al interface active sites, while the high HDO/DCO value was ascribed to two aspects, i.e., abundant B acid sites on the surface of the outer silica shell and its core-shell structure containing inner metallic Pd core and outer silica shell doped with aluminum atoms.

4. Conclusions

In this work, to solve the problems that traditional supported-palladium catalysts are prone to cause the cleavage of C-C bonds and occur agglomeration during the conversion of fatty acid esters, we prepared an efficient and stable Pd@Al_x-mSiO₂ core-shell nanocatalysts doped with aluminum atoms. Under the mild reaction conditions (260 °C and 3.0 MPa), the optimized Pd@Al₃-mSiO₂ not only exhibited high HDO activity and selectivity towards diesel-range alkanes, but also showed good stability with a slight loss (conversion decreased from 98% to 90%) over five cycles. The structure-activity relationship based on the detailed characterization (TEM, HRTEM, ²⁷Al NMR NH₃-TPD, and in situ FTIR) indicates that the high catalytic performance of Pd@Al₃-mSiO₂ mainly results from the cooperative effects of uniformly dispersed



Scheme 2. (a) Surface reaction model for the hydrodeoxygenation of fatty esters over the Pd@Al_x-mSiO₂ catalyst; (b) Surface reaction model for the deoxygenation of fatty aldehyde intermediates over the Pd/ γ -Al₂O₃ catalyst.

Pd metal, Lewis- and Brønsted-acid sites generated through the formation of Si—OH—Al bonds, while the good stability of Pd@Al₃-mSiO₂ was ascribed to its unique core-shell structure, inhibiting the leaching and agglomeration of metallic Pd nanoparticles during the reaction.

CRedit authorship contribution statement

Xincheng Cao: Validation, Formal analysis, Investigation, Writing – original draft. **Jiaping Zhao:** Methodology, Formal analysis. **Feng Long:** Conceptualization, Methodology. **Xiaolei Zhang:** Validation, Formal analysis. **Junming Xu:** Conceptualization, Methodology, Formal analysis, Writing – review & editing. **Jianchun Jiang:** Conceptualization, Methodology, Writing – review & editing.

Declaration of Competing Interest

The authors declare that they have no known competing financial interests or personal relationships that could have appeared to influence the work reported in this paper.

Acknowledgements

The authors would like to thank the financial support provided by the National Natural Science Foundation of China (2019YFB1504005 and 2019YFB1504000).

Appendix A. Supporting information

Supplementary data associated with this article can be found in the online version at doi:10.1016/j.apcatb.2022.121068.

References

- [1] C. Kordulis, K. Bourikas, M. Gousi, E. Kordouli, A. Lycourghiotis, Development of nickel based catalysts for the transformation of nature triglycerides and related compounds into green diesel: a critical review, *Appl. Catal. B: Environ.* 181 (2016) 156–196.
- [2] B. Ma, C. Zhao, High-grade diesel production by hydrodeoxygenation of palm oil over a hierarchically structured Ni/HBEA catalyst, *Green Chem.* 17 (2015) 1692–1701.
- [3] F. Jamil, L. Al-Haj, A.H. Al-Muhtaseb, M.A. Al-Hinai, M. Baawain, U. Rashid, M.N. M. Ahmad, Current scenario of catalysts for biodiesel production: a critical review, *Rev. Chem. Eng.* 34 (2018) 267–297.
- [4] C. Zhao, T. Bruck, J.A. Lercher, Catalytic deoxygenation of microalgae oil to green hydrocarbons, *Green Chem.* 15 (2013) 1720–1739.
- [5] J. Li, J.J. Zhang, S. Wang, G.G. Xu, H. Wang, D.G. Vlachos, Chemoselective hydrodeoxygenation of carboxylic acids hydrocarbons over nitrogen-doped carbon-alumina hydride-supported iron catalysts, *ACS Catal.* 9 (2019) 1564–1577.
- [6] D. Kubicka, L. Kaluza, Deoxygenation of vegetable oils over sulfided Ni, Mo and NiMo catalysts, *Appl. Catal. A: Gen.* 372 (2010) 199–208.
- [7] Y.Y. Liu, R. Sotelo-Boyás, K. Murata, T. Minowas, K. Sakanishi, Hydrotreatment of vegetable oils to produce bio-hydrogenated diesel and liquefied petroleum gas fuel over catalysts containing sulfided Ni-Mo and solid acids, *Energy Fuels* 25 (2011) 4675–4685.
- [8] H. Wang, G.L. Li, K. Rogers, H.F. Lin, Y. Zheng, S. Ng, Hydrotreating of wasting cooking oil over supported CoMoS catalysts-catalyst deactivation mechanism study, *Mol. Catal.* 443 (2017) 228–240.
- [9] R.G. Kukushkin, O.A. Bulavchenko, V.V. Kaichev, V.A. Yakovlev, Influence of Mo on catalytic activity of Ni-based catalysts in hydrodeoxygenation of esters, *Appl. Catal. B: Environ.* 163 (2015) 531–538.
- [10] X. Yu, J. Chen, T. Ren, Promotional effect of Fe on performance of Ni/SiO₂ for deoxygenation of methyl laurate as a model compound to hydrocarbons, *RSC Adv.* 4 (2014) 46427–46436.
- [11] J. Chen, H. Shi, L. Li, K. Li, Deoxygenation of methyl laurate as a model compound to hydrocarbons on transition metal phosphide catalysts, *Appl. Catal. B: Environ.* 144 (2014) 870–884.
- [12] Y. Zhou, X. Liu, P. Yu, C. Hu, Temperature-tuned selectivity to alkanes or alcohol from ethyl palmitate deoxygenation over zirconia-supported cobalt catalyst, *Fuel* 278 (2020) 1–13.
- [13] Y. Zhou, L. Liu, G. Li, C. Hu, Insights into the influence of ZrO₂ crystal structures on methyl laurate hydrogenation over Co/ZrO₂ catalysts, *ACS Catal.* 11 (2021) 7099–7113.
- [14] Z. Zhang, M. Jing, H. Chen, F. Okeji, J. Liu, Y. Leng, H.L. Liu, W.Y. Song, Z. Y. Hou, X.Y. Lu, J. Fu, J. Liu, Transfer hydrogenation of fatty acids on Cu/ZrO₂: demystifying the role of carrier structure and metal-support interface, *ACS Catal.* 10 (2020) 9098–9108.
- [15] Q. Xia, X. Zhuang, M.M.-J. Li, Y.-K. Peng, G. Liu, T.S. Wu, Y.-L. Soo, X.Q. Gong, Y. Wang, S.C.E. Tsang, Cooperative catalysis for direct hydrodeoxygenation of vegetable oils into diesel-range alkanes over Pd/NbOPO₄, *Chem. Commun.* 52 (2016) 5160–5163.
- [16] A. Srifa, K. Faungnawakij, V. Itthibenchapong, S. Assabumrungrat, Roles of monometallic catalysts in hydrodeoxygenation of palm oil to green diesel, *Chem. Eng. J.* 278 (2015) 249–258.
- [17] N. Chen, Y. Ren, E.W. Qian, Elucidation of the active phase in PtSn/SAPO-11 for hydrodeoxygenation of methyl palmitate, *J. Catal.* 334 (2016) 79–88.
- [18] S. Liu, T. Simonetti, W. Zheng, B. Saha, Selective hydrodeoxygenation of vegetable oils and waste cooking oils to green diesel using a silica-supported Ir-ReO_x bimetallic catalyst, *ChemSusChem* 11 (2018) 1446–1454.
- [19] Z.Y. Pan, R.J. Wang, J.X. Chen, Deoxygenation of methyl laurate as a model compound on Ni-Zn alloy and intermetallic compound catalysts: geometric and electronic effects of oxophilic Zn, *Appl. Catal. B: Environ.* 224 (2018) 88–100.
- [20] A.J. Porkovich, P. Kumar, Z. Ziadi, D.C. Lloyd, L. Weng, N. Jian, T. Sasaki, M. Sowwan, A. Datta, Defect-assisted electronic metal-support interactions: tuning the interplay between Ru nanoparticles and CuO supports for pH-neutral oxygen evolution, *Nanoscale* 13 (2021) 71–80.
- [21] C. Wang, L. Wang, J. Zhang, H. Wang, J.P. Lewis, F.S. Xiao, Product selectivity controlled by zeolite crystals in biomass hydrogenation over a palladium catalyst, *J. Am. Chem. Soc.* 138 (2016) 7880–7883.
- [22] P. Zhang, H. Wu, M. Fan, W. Sun, P. Jiang, Y. Dong, Direct and postsynthesis of tin-incorporated SBA-15 functionalized with sulfonic acid for efficient biodiesel production, *Fuel* 235 (2019) 426–432.
- [23] J. Pu, K. Nishikado, N. Wang, T.T. Nguyen, T. Maki, E.W. Qian, Core-shell nickel catalysts for the steam reforming of acetic acid, *Appl. Catal. B: Environ.* 224 (2018) 69–79.
- [24] M. Lv, Y. Zhang, Q. Xin, D. Yin, S.T. Yu, S.W. Liu, L. Li, C.X. Xie, Q. Wu, H.L. Yu, Y. Liu, Pd@ Al-containing mesoporous silica yolk-shell-structured nanospheres as high performance nanoreactors for the selective hydrolysis of glucose to 1, 2-propylene glycol, *Chem. Eng. J.* 396 (2020) 1–12.
- [25] R.P. Ye, X.Y. Wang, C.-A. Hurd Price, X.Y. Liu, Q.H. Yang, M. Jaroniec, J. Liu, Engineering of yolk/core-shell structured nanoreactors for thermal hydrogenations, *Small* 17 (2021) 1–23.
- [26] H. Ghasemi Mobtaker, S.J. Ahmadi, S. Moradi Dehaghi, T. Yousefi, Coupling system application in photocatalytic degradation of methylorange by TiO₂, TiO₂/SiO₂ and TiO₂/SiO₂/Ag, *Rare Met.* 34 (2015) 851–858.
- [27] M. Lv, Q. Xin, B. Bian, S. Yu, S. Liu, L. Li, X.C. Xie, Y. Liu, One-pot synthesis of highly active and hydrothermally stable Pd@ mHSiO₂ yolk-shell-structured nanoparticles for high-temperature reactions in hydrothermal environments, *Dalton Trans.* 49 (2020) 418–430.
- [28] S.H. Joo, J.Y. Park, C.K. Tsung, Y. Yamada, P. Yang, G.A. Somorjai, Thermally stable Pt/mesoporous silica core-shell nanocatalysts for high-temperature reactions, *Nat. Mater.* 8 (2009) 126–131.
- [29] X. Guo, X.Q. Sun, Y. Guo, Y.L. Guo, Y.S. Wang, L. Wang, W.C. Zhan, Enhanced catalytic performance for selective oxidation of propene with O₂ over bimetallic Au-Cu/SiO₂ catalysts, *Rare Met.* 40 (2021) 1056–1066.
- [30] N. Chen, S. Gong, H. Shirai, T. Watanabe, E.W. Qian, Effects of Si/Al ratio and Pt loading on Pt/SAPO-11 catalysts in hydroconversion of Jatropha oil, *Appl. Catal. A: Gen.* 466 (2013) 105–115.
- [31] K. Kon, W. Onodera, S. Takakusagi, Ki Shimizu, Hydrodeoxygenation of fatty acids and triglycerides by Pt-loaded Nb₂O₅ catalysts, *Catal. Sci. Technol.* 4 (2014) 3705–3712.
- [32] X.C. Cao, F. Long, Q.L. Zhai, P. Liu, J.M. Xu, J.C. Jiang, Enhancement of fatty acids hydrodeoxygenation selectivity to diesel-range alkanes over the supported Ni-MoO_x catalyst and elucidation of the active phase, *Renew. Energy* 162 (2020) 2113–2125.
- [33] M. Trombetta, G. Busca, M. Lenarda, L. Storato, M. Pavan, An investigation of the surface acidity of mesoporous Al-containing MCM-41 and of the external surface of ferrierite through pivalonitrile adsorption, *Appl. Catal. A: Gen.* 182 (1999) 225–235.
- [34] B. Dragoi, E. Dumitriu, C. Guimon, A. Auroux, Acidic and adsorptive properties of SBA-15 modified by aluminum incorporation, *Microporous Mesoporous Mater.* 121 (2009) 7–17.
- [35] Y. Li, D. Pan, C. Yu, Y. Fan, X. Bao, Synthesis and hydrosulfurization properties of NiW catalyst supported on high-aluminum-content, highly ordered, and hydrothermally stable Al-SBA-15, *J. Catal.* 286 (2012) 124–136.
- [36] F. Wang, J. Jiang, K. Wang, Q. Zhai, F. Long, P. Liu, F.J. Feng, H.H. Xia, J. Ye, J. Li, J.M. Xu, Hydrotreatment of lipid model for diesel-like alkane using nitrogen-doped mesoporous carbon-supported molybdenum carbide, *Appl. Catal. B: Environ.* 242 (2019) 150–160.
- [37] Y. Xiao, Q. Meng, X. Pan, C. Zhang, Z. Fu, C. Li, Selective production of bio-based para-xylene over an FeO_x-modified Pd/Al₂O₃ catalyst, *Green Chem.* 22 (2020) 4341–4349.
- [38] H. Sun, J. Han, Y. Ding, W. Li, J. Duan, P. Chen, H. Lou, X.M. Zheng, One-pot synthesized mesoporous Ca/SBA-15 solid base for transesterification of sunflower oil with methanol, *Appl. Catal. A: Gen.* 390 (2010) 26–34.
- [39] J. Jiao, J. Fu, Y. Wei, Z. Zhao, A. Duan, C.M. Xu, J.M. Li, H. Song, P. Zheng, X. L. Wang, Y.N. Yang, Y. Liu, Al-modified dendritic mesoporous silica nanospheres-supported NiMo catalysts for the hydrosulfurization of dibenzothiophene: efficient accessibility of active sites and suitable metal-support interaction, *J. Catal.* 356 (2017) 269–282.
- [40] J. Pérez-Pariente, J. Sanz, V. Fornés, A. Corma, ²⁹Si and ²⁷Al MAS NMR study of zeolite β with different Si/Al ratios, *J. Catal.* 124 (1990) 217–223.

- [41] O.M. Busch, W. Brijoux, S. Thomson, F. Schüth, Spatially resolving infrared spectroscopy for parallelized characterization of acid sites of catalysts via pyridine sorption: possibilities and limitations, *J. Catal.* 222 (2004) 174–179.
- [42] G. Wu, N. Zhang, W. Dai, N. Guan, L. Li, Construction of bifunctional Co/H-ZSM-5 catalysts for the hydrodeoxygenation of stearic acid to diesel-range alkanes, *ChemSusChem* 11 (2018) 2179–2188.
- [43] G. Cui, X. Meng, X. Zhang, W. Wang, S. Xu, Y.C. Ye, K.J. Tang, W.M. Wang, J. H. Zhu, M. Wei, D.G. Evans, X. Duan, Low-temperature hydrogenation of dimethyl oxalate to ethylene glycol via ternary synergistic catalysis of Cu and acid-base sites, *Appl. Catal. B: Environ.* 248 (2019) 394–404.
- [44] A. Ali, B. Li, Y. Lu, C. Zhao, Highly selective and low-temperature hydrothermal conversion of natural oils to fatty alcohols, *Green Chem.* 21 (2019) 3059–3064.
- [45] G. Xu, Y. Zhang, Y. Fu, Q. Guo, Efficient hydrogenation of various renewable oils over Ru-HAP catalyst in water, *ACS Catal.* 7 (2017) 1158–1169.
- [46] A. Dandekar, M.A. Vannice, Crotonaldehyde hydrogenation on Pt/TiO₂ and Ni/TiO₂ SMSI catalysts, *J. Catal.* 183 (1999) 344–354.